

Electrophoretic Deposition, Microstructure, and Corrosion Resistance of Porous Sol–Gel Glass/Polyetheretherketone Coatings on the Ti-13Nb-13Zr Alloy



TOMASZ MOSKALEWICZ, ANITA ZYCH, ALICJA ŁUKASZCZYK, KATARZYNA CHOLEWA-KOWALSKA, ADAM KRUK, BEATA DUBIEL, AGNIESZKA RADZISZEWSKA, KATARZYNA BERENT, and MARTA GAJEWSKA

In this study, microporous composite sol–gel glass/polyetheretherketone (SGG/PEEK) coatings were produced on the Ti-13Nb-13Zr titanium alloy by electrophoretic deposition. Coatings with different levels of high open porosity were developed by introducing SGG particles of varying diameters into the PEEK matrix. The microstructure of the coatings was characterized by electron microscopy and X-ray diffractometry. The coatings with 40–50 μm thickness were composed of semicrystalline SGG particles consisting of hydroxyapatite, CaSiO_3 , some Ca_2SiO_4 , and an amorphous phase containing Ca, Si, P, and O, homogeneously embedded in a semicrystalline PEEK matrix. The size of SGG particles present in the coatings strongly influenced the formation of microcracks and their adhesion to the underlying substrate. Microscratch tests showed that the coating containing SGG particles with a diameter smaller than 45 μm and open porosity of 45 pct exhibited good adhesion to the titanium alloy substrate, much better than the coating containing particles with a diameter smaller than 85 μm and total open porosity equal to 48 pct. The corrosion resistance was investigated in Ringer's solution at a temperature of 310 K (37 °C) for a pH equal to 7.4 and in deaerated solutions with the use of open-circuit potential, potentiodynamic polarization, and electrochemical impedance spectroscopy. The SGG/PEEK-coated alloy indicated better electrochemical corrosion resistance compared with the uncoated alloy.

DOI: 10.1007/s11661-017-4030-0

© The Author(s) 2017. This article is published with open access at Springerlink.com

I. INTRODUCTION

TITANIUM alloys are the most frequently used metallic materials for biomedical applications due to their high strength-to-weight ratio, high fatigue resistance, and good biocompatibility.^[1,2] Today, the most important titanium alloys, which have found applications in medicine, are β alloys. They exhibit low elastic modulus and density, high strength, and ductility as well as good electrochemical corrosion resistance.^[3–5] However, their use in medicine is limited not only by their

relatively low hardness and poor tribological properties, but also by the very slow osseointegration between implants and surrounding bone tissues.^[6,7] Titanium alloy osseointegration might be enhanced by surface treatment involving the deposition of porous coatings containing bioceramics, biopolymers, and their combinations. The porous coatings improve osseointegration by providing more space for bone growth. Moreover, the bond between the biomaterial and bone becomes stronger.^[8,9] Porosity, pore diameter, distribution, and interconnectivity are important parameters, which determine the biomaterial bioactivity.^[10] In general, open porosity higher than 50 pct and interconnected pores with a mean diameter of 100 μm or higher are considered to be the minimum requirements to permit tissue ingrowth.^[11,12] For example, Hadjicharalambous *et al.*^[13] showed that about 50 pct porosity and an average pore size of 150 μm are beneficial for cellular growth in zirconia ceramics. The important limitations to the use of materials, especially ceramics, with high porosity and pore size are their low mechanical properties.^[14] Thus, a good response to the improvement of the mechanical properties of highly porous coatings may be the introduction of a polymer and the deposition of composite polymer-based coatings incorporating ceramic particles.

TOMASZ MOSKALEWICZ, ANITA ZYCH, ADAM KRUK, BEATA DUBIEL, and AGNIESZKA RADZISZEWSKA are with the Faculty of Metals Engineering and Industrial Computer Science, AGH University of Science and Technology, Czarnowiejska 66, 30-054 Kraków, Poland. Contact e-mail: tmoskale@agh.edu.pl ALICJA ŁUKASZCZYK is with the Faculty of Foundry Engineering, AGH University of Science and Technology, Reymonta 23, 30-059 Kraków, Poland. KATARZYNA CHOLEWA-KOWALSKA is with the Faculty of Materials Science and Ceramics, AGH University of Science and Technology, Mickiewicza Av. 30, 30-059 Kraków, Poland. KATARZYNA BERENT and MARTA GAJEWSKA are with the Academic Centre for Materials and Nanotechnology, AGH University of Science and Technology, Mickiewicza Av. 30, 30-059 Kraków, Poland.

Manuscript submitted December 5, 2016.

Article published online February 27, 2017

Electrophoretic deposition (EPD) is a surface engineering method, which enables the codeposition of different ceramic or/and polymeric materials, producing dense or porous composite polymer-based coatings with high homogeneity and tailored thickness.^[15,16] EPD consists of the movement of charged particles suspended in liquid and deposition onto a conducting substrate under the influence of an externally applied electrical field.^[17,18] The advantages of this method are high purity, easy control of the coating thickness, high coating uniformity, the possibility of using complex shaped substrates, and the short deposition time of coatings.^[19,20]

One of the popular materials with useful properties for a relatively strong porous coating matrix is polyetheretherketone (PEEK). PEEK is a nontoxic and bioinert material.^[16,21,22] It is a crystallizable aromatic polymer with very good thermal and mechanical properties. This polymer is used to replace metal implant components, especially in long-term orthopedic applications.^[23] Furthermore, PEEK is noncytotoxic and can be repeatedly sterilized without evident deterioration of its mechanical properties.^[21]

The osseointegration process of titanium alloy might be enhanced by using a bioactive glass or glass-ceramic as a bioactive coating component. A typical feature common to all bioactive glasses, both melt or sol-gel derived, is the ability to interact with living tissue, in particular forming strong bonds to bone.^[24] Bioactive glasses are amorphous silicate-based materials exhibiting osteoconductive/osteoinductive properties.^[10,25,26] They are promising materials for bone tissue engineering applications due to their excellent bioactivity, biocompatibility, and osteogenicity properties.^[27,28] Bioactive glass stimulates new bone growth and, once implanted in the body, can react with physiological fluids and form a strong bond with bones. Its bioactivity is associated with the formation of a carbonated hydroxyapatite layer (HCA) on its surface, similar to the bone mineral.^[29,30]

Glass-ceramics with crystalline or semicrystalline structures are produced by the transformation of the glass into a ceramic.^[10] The sol-gel glasses offer several advantages compared with the melt-delivered glasses. Due to their nonporous texture, the sol-gel-derived glasses exhibit a high specific surface area in comparison with melt-delivered glasses. The most significant advantage of sol-gel glasses is the presence of Si-OH groups in their structure, which are thought to play a role in HCA layer nucleation.^[10] Thus, their bioactivity is usually higher than that of bioactive glasses prepared by melting.^[31] Gel-derived bioactive glasses influence the faster formation of a strong bond with tissue, and also stimulate bone into regeneration.^[32]

According to our knowledge, there are very few papers available in the literature on the EPD of composite bioglass/PEEK coatings.^[15,33] The main focus of the referred studies was the investigation of EPD parameters and the final quality of the composite coatings. However, there is no information about the EPD of sol-gel glass/PEEK coatings. The originality of this study is incorporation of the gel-derived glass-ceramic with a high surface area into the PEEK matrix

and deposition of microporous coatings on near- β titanium alloy, as well as comparison of the sol-gel glass/PEEK coating microstructures and adhesion behaviors to the substrate with the bioglass/PEEK coatings deposited in our previous study.^[33]

The aim of this study was electrophoretic deposition of microporous SGG/PEEK coatings on the Ti-13Nb-13Zr alloy, as well as the characterization of the microstructure and selected properties, such as adhesion of the coatings to the titanium alloy substrate and electrochemical corrosion resistance in Ringer's solution.

II. METHODS AND MATERIALS

Composite sol-gel glass SGG/PEEK coatings were electrophoretically deposited on a near- β Ti-13Nb-13Zr alloy. The alloy, in the shape of a bar, was delivered by Xi'an Saite Metal Materials Development Co., Ltd., China. The microstructure of the alloy was described in detail in our previous paper.^[34] It was composed of α' (hexagonal close-packed; hcp), β (body-centered cubic; bcc), and a small amount of α'' phase (orthorhombic, Cmc_m space group). Disks of 27 mm diameter and 2 mm thickness were used as substrates for EPD. The samples were ground with sandpaper of 2000 grit and then cleaned with distilled water and ethanol.

The PEEK powder and SGG particles were used as coating components. The PEEK powder (VICOTE[®]704) was delivered by Victrex Europa GmbH, Germany. It has a melting point of about 616 K (343 °C), a crystallization peak at 433 K (160 °C), and a glass transition temperature of 416 K (143 °C). The bioactive sol-gel glass with nominal composition (mol pct) 54CaO-6P₂O₅-40SiO₂ (A2) was produced by the sol-gel method described previously in the literature.^[27,31] In the alcohol-based system, the following compounds were used as the starting materials: tetraethylorthosilicate (TEOS, Si(OC₂H₅)₄), triethylphosphate (TEP, OP(OC₂H₅)₃) (Sigma-Aldrich, USA), and calcium nitrate tetrahydrate (Ca(NO₃)₂·4H₂O) (POCH, Poland). HCl solution (1 M) (POCH, Poland) and distilled water were applied as the catalyst of the hydrolysis and polycondensation reactions. In brief, the first step was to mix and stir TEOS and ethanol in particular amounts. Subsequently, the appropriate volumes of distilled water and hydrochloric acid were added to the mixture, and next the TEP and calcium nitrate (dissolved in distilled water) were added gradually to the solution. After the addition of each reactant, the solution was stirred for 1 hour at room temperature (RT). The final solution was left at RT until the gel was formed. Subsequently, the gel was dried at 353 K (80 °C) for 72 hours and then heated up to 973 K (700 °C) for 20 hours. Afterward, it was sieved to obtain sol-gel glass powders with two different particle sizes: SGG1 with a diameter up to 45 μ m and SGG2 with a diameter up to 85 μ m. The SGG1 and SGG2 powders were used as a component materials for the EPD of composite coatings.

Different suspensions of SGG and PEEK powder in ethanol were used for coating deposition. They were prepared by adding 3.2-3.5 g of SGG1 or SGG2, 1.5 g

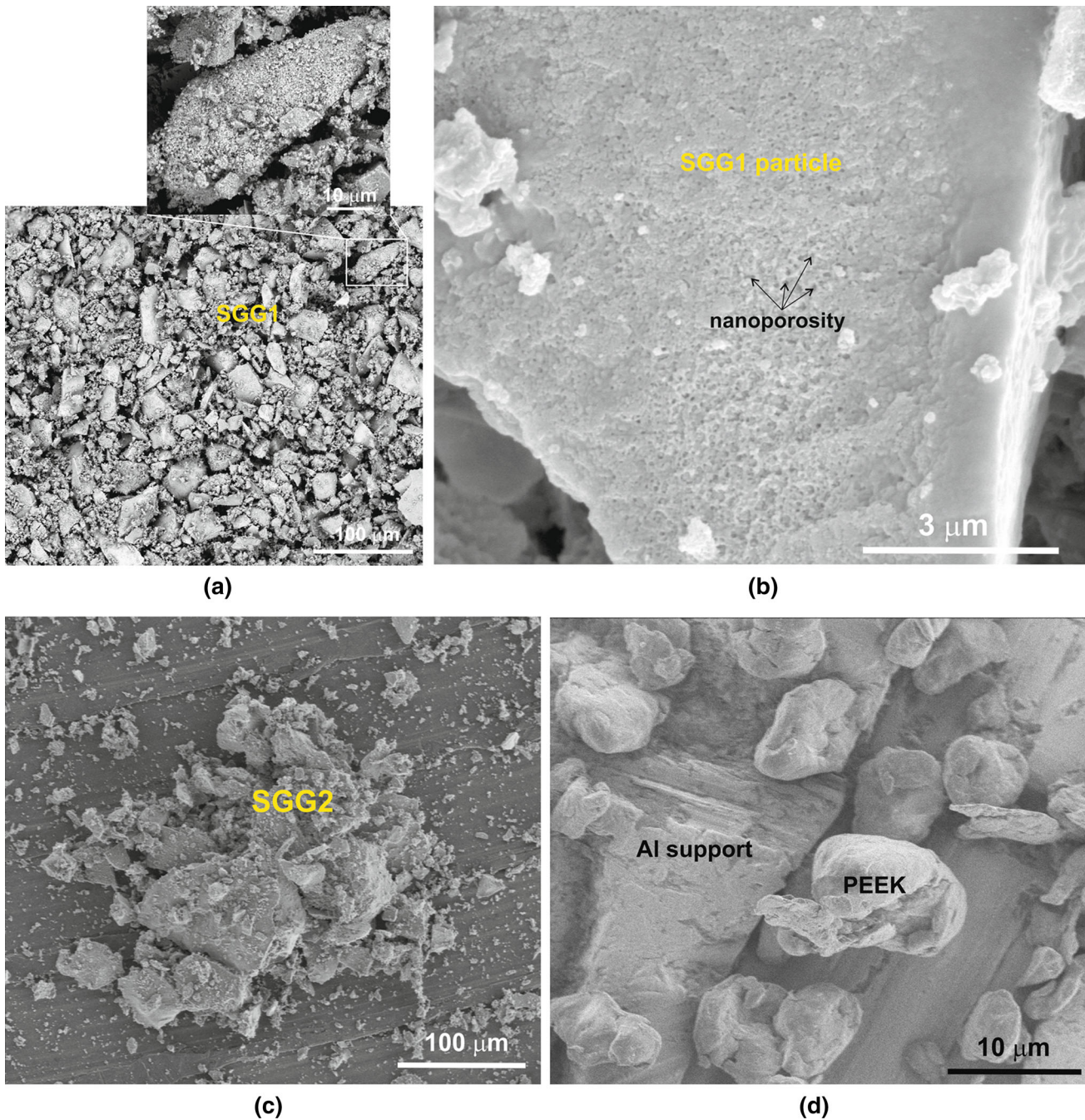


Fig. 1—SEM micrographs of the materials used for EPD of composite coatings: (a) backscattered electron (BSE) image of the SGG1 particles. An inset shows magnified details of the representative particle; (b) nanoporosity in the SGG1 particles, secondary electron (SE) image; (c) BSE image of the SGG2 particles; (d) SE image of the PEEK particles.

of PEEK powder, and 1-5 g of citric acid to the 50 mL of ethanol and sonicating the mixture in an ultrasonic bath for 5 minutes in order to disperse the particles. Before deposition, the suspensions were mixed for 3 minutes using a magnetic stirrer. The pH values were measured using a Mettler Toledo EL20 pH-meter (China). The changes of pH in the suspensions were realized by adding different amounts of citric acid ($C_6H_8O_7$). The EPD was carried out under constant voltage in the range of 30-70 V, and the deposition time ranged from 60 to 120 seconds. The distance between

electrodes in the EPD cells was maintained at 10 mm. After EPD, the coated samples were dried at room temperature and subsequently heated at a temperature of 628 K (355 °C) for 20 minutes, heating rate 7.9 K/min (4.5 °C/min), then cooled using the furnace.

The microstructure of the coatings was investigated by scanning and transmission electron microscopy (SEM, TEM) as well as X-ray diffractometry (XRD). The SEM investigation was performed using a Nova NanoSEM 450 (FEI, the Netherlands). The TEM investigation was carried out using a JEOL JEM-2010

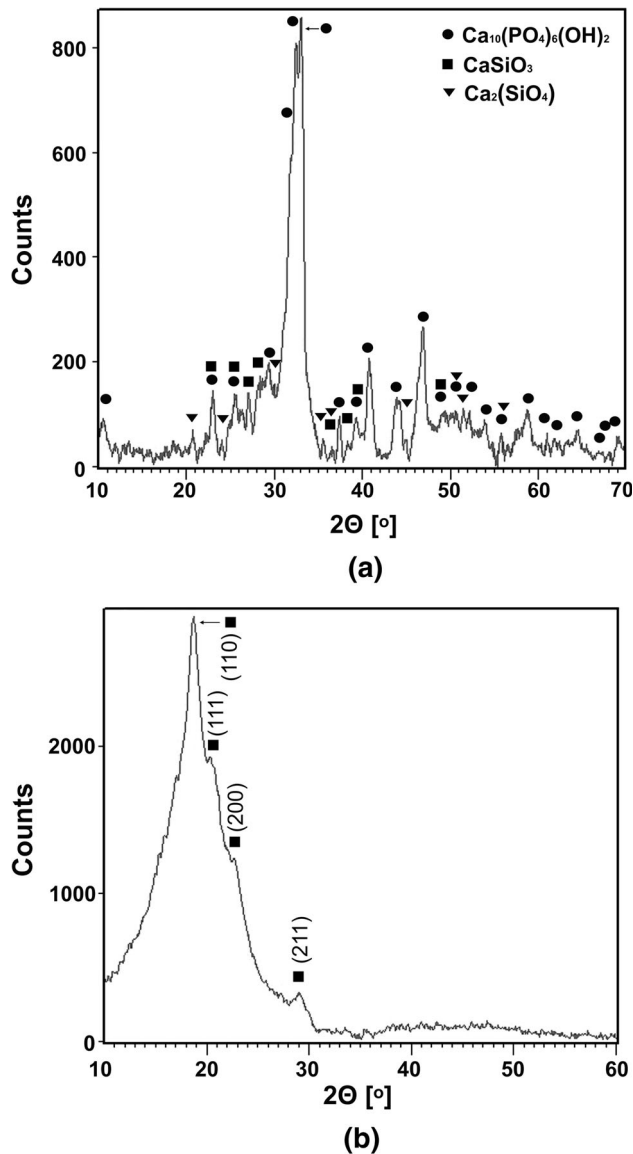


Fig. 2—XRD patterns of the SGG (a) and the PEEK (b) powders used for EPD as well as their identification.

ARP microscope (Japan). The cross-sectional lamella for TEM investigation of coating microstructure was prepared by a focus ion beam (FIB) using an FEI QUANTA 3D 200i device (the Netherlands). Phase identification was performed by means of selected area electron diffraction (SAED) and XRD (Bragg-Brentano method). The XRD patterns were recorded using a Panalytical Empyrean DY 1061 diffractometer (the Netherlands). The diffractometer was operated with Cu $K\alpha$ radiation at the 2θ range of 10 to 70 deg, using plan-view specimens. The total open porosity was determined by hydrostatic weighing based on the Archimedes principle.^[35] The test was performed for three porous specimens, and the average value was calculated. Tomographic datasets were obtained using the “slice and view” technique using a FEI Versa 3D dual-beam scanning electron microscope (the

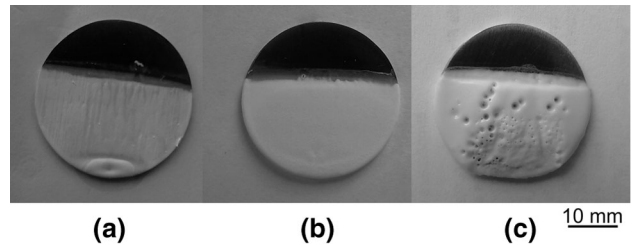


Fig. 3—Macroscopic images of the SGG1/PEEK coatings deposited at a constant voltage of 50 V for 120 s from suspensions with different concentrations of SGG1: (a) 3 g, (b) 3.2 g, (c) 3.5 g.

Netherlands) equipped with the AutoSlice and View™ G3 software. A regular cross section was milled using a Ga⁺ LMIS source at 30 kV and an ion current of 1 nA, and a voxel size of $36 \times 36 \times 120$ nm. SEM imaging with an ETD detector at 5 kV was applied for 3D visualization of open porous SGG1/PEEK coating. The digital processing of data stacks and 3D visualization of reconstructed volume were performed using ImageJA 1.45b and Avizo Fire 6.3 software. The coating thickness was measured by contact profilometry using a CSM Instruments Micro-Combi Tester (MCT), Switzerland. The 5-mm trace length started in the uncoated area and finished on the coating surface. The difference in the recorded heights in these areas was equal to the coating thickness.

The adhesion of the coatings to the titanium alloy was investigated by the microscratch test method using the MCT. The microscratch tests were carried out using a Rockwell C indenter with a cone apex angle of 120 deg and tip radius of 200 μm . Tests were performed within the distance of 5 mm and with a load of 30 N. The critical loads L_{c1} (cohesive cracks) and L_{c2} (adhesive cracks) were determined from light microscopy (LM) observations, acoustic emission, and friction force signals. Average values of critical loads were calculated from three scratches.

The electrochemical studies of the samples were carried out using an Autolab PGSTAT302N potentiostat (the Netherlands). Ringer’s solution was used as the electrolyte for the corrosion study. The chemical composition of Ringer’s solution was as follows: 8.6 g NaCl, 0.3 g KCl, and 0.25 g CaCl₂. The tests were carried out at a temperature of 310 K (37 °C). Electrochemical measurements were performed for a pH equal to 7.4 and in deaerated solutions. The linear sweep voltamperometry curves were recorded at a scan rate of 1 mV/s in the potential range from -1.3 to $+1.5$ V. The investigations were performed using a classical three-electrode cell, where the working electrode was a titanium alloy. Potentials were measured vs saturated calomel electrode (SCE), and the counter electrode was made of platinum wire. Electrochemical impedance spectra were acquired at the open-circuit potential. The amplitude of the perturbation signal was 10 mV, and EIS spectra were plotted in the frequency range from 10^5 to 10^{-3} Hz. The EIS data were fitted using the ZView software.

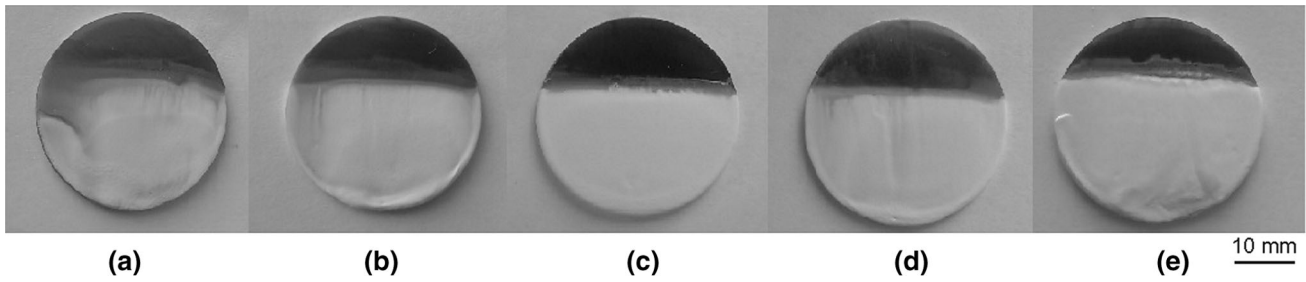


Fig. 4—Macroscopic images of the SGG1/PEEK coatings deposited from the suspension composed of 3.2 g SGG1, 1.5 g PEEK, and 5 g citric acid in 50 mL of EtOH for 120 s at different voltages: (a) 30 V, (b) 40 V, (c) 50 V, (d) 60 V, (e) 70 V.

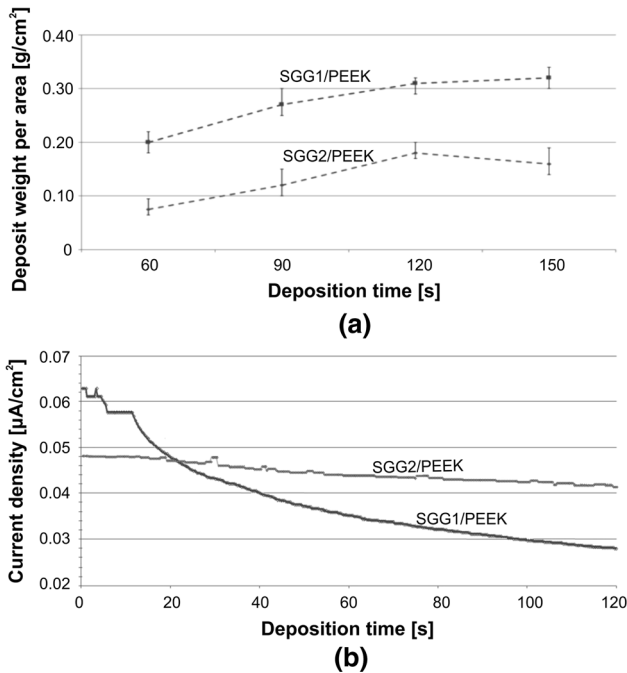


Fig. 5—The deposit weight vs deposition time during the EPD of the SGG1/PEEK and SGG2/PEEK coatings at a constant voltage of 50 V (a) as well as the effects of deposition time on current density during the EPD of the SGG1/PEEK and SGG2/PEEK coatings (b).

III. RESULTS AND DISCUSSION

A. Electrophoretic Codeposition of SGG and PEEK

The electrophoretic deposition depends on (i) parameters related to the suspension including chemical composition, morphology, and particle size and the type of solvent, as well as (ii) the physical conditions of the deposition process such as potential difference and time. Particle size and morphology are important parameters of the EPD process. For stable suspensions, it is important that the particles remain well dispersed and stable to form homogeneous and uniform deposits. The problem with large particles, with a diameter greater than $\sim 20 \mu\text{m}$, is the tendency to undergo sedimentation.^[36] It is difficult to obtain uniform deposition from a sedimenting suspension of large particles.^[37] Therefore, continuous stirring of suspensions containing large particles is required during the coating

deposition. To deposit coatings with different open porosity, two types of relatively large SGG particles with equivalent circle diameters of (ECD)—SGG1 $< 45 \mu\text{m}$ and SGG2 $< 85 \mu\text{m}$ —were used for the EPD of coatings in the present study.

The representative SEM images of SGG1 and SGG2 particles are given in Figures 1(a) through (c). Both types of SGG particles exhibited an irregular shape, nanoporosity (Figure 1(c)), and a high specific surface area (as shown in the magnified inset in Figure 1(a)). XRD analyses of SGG (SGG1 and SGG2) revealed the presence mainly of hydroxyapatite $\text{Ca}_{10}(\text{PO}_4)_6(\text{OH})_2$ (hexagonal primitive; hp) and CaSiO_3 (triclinic primitive; tp) phases. The occurrence of a Ca_2SiO_4 (orthorhombic primitive; op) phase is also possible as seen from the XRD analysis. The XRD pattern for SGG1 is shown in Figure 2(a). The presence of some broad peaks in the XRD pattern also indicates the possible existence of an amorphous phase. The mean chemical composition of SGG detected by SEM-EDS microanalysis was the following (in at. pct) 19.2 Ca, 20.5 Si, 4.9 P, and O the balance.

The PEEK powder exhibited a nearly amorphous structure (Figure 2(b)); however, a low amount of crystalline phase was also present. Four weak diffraction peaks at 2θ angles of 18.68, 20.74, 22.92, and 29.15 deg occurred in the spectrum. The particles had a nearly spherical shape and ECD ranging from 2 to $15 \mu\text{m}$ (Figure 1(d)).

Electrophoretic codepositions of SGG and PEEK particles were carried out from the EtOH-based suspensions. During EPD, both the SGG and the PEEK particles were positively charged and moved toward the cathode (substrate material) under the electric field. Due to the large sizes of both the SGG and the PEEK particles, it was impossible to measure their zeta potential and electrophoretic mobility in EtOH using the laser Doppler microelectrophoresis method. Thus, the suspension's chemical composition and EPD parameters were selected by trial and error. A similar chemical composition of the suspension, as well as similar deposition voltage and time to that used in our previous study for deposition of the bioglass/PEEK coatings on the Ti-6Al-7Nb alloy,^[33] was applied.

A series of coatings were deposited using suspensions with different concentrations of SGG1 or SGG2 powders (3, 3.2, and 3.5 g) and citric acid (1, 2, 3, 4, and 5 g) in 50 mL of EtOH at a potential difference in the range

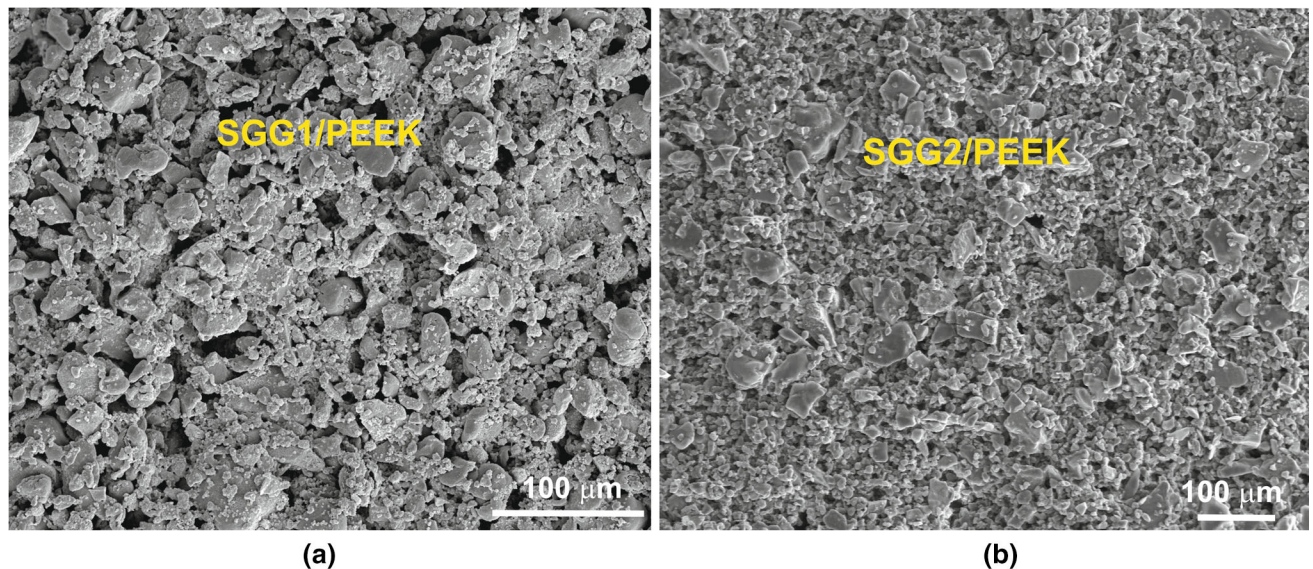


Fig. 6—SEM SE micrographs of the as-deposited SGG1/PEEK (a) and SGG2/PEEK (b) coatings on the Ti-13Nb-13Zr alloy.

of 30 to 70 V and different deposition times of 60, 90, 120, and 150 seconds. Selected macroscopic images of the SGG1/PEEK coating deposited on the titanium alloy at a constant voltage of 50 V for 120 seconds from suspensions with different contents of SGG1 equal to 3, 3.2, and 3.5 g are shown in Figures 3(a) through (c), respectively. The macroscopically homogeneous coating was deposited from the suspension contains 3.2 g of SGG1 (Figure 3(b)).

Figures 4(a) through (e) show the macroscopic images of the SGG1/PEEK coatings deposited from a suspension of 3.2 g of SGG1, 1.5 g of PEEK, and 5 g of citric acid in 50 mL of EtOH at different deposition voltage and a constant time equal to 120 seconds. The visual observation of the coated specimens showed that the most uniform SGG1/PEEK and SGG2/PEEK coatings were deposited from a suspension of 3.2 g of SGG1 or SGG2, 1.5 g of PEEK, and 5 g of citric acid in 50 mL of EtOH (pH 2.84 and 2.91, respectively) applying a constant voltage of 50 V and a deposition time of 120 seconds. The coatings deposited at the lower voltage of 30 and 40 V were not uniformly distributed on the substrate. Frequently, the discontinuities of the coatings were observed, and thus they did not cover tightly the surface of the underlying alloy. At higher voltages of 60 and 70 V, the coatings were thicker but inhomogeneous in thickness.

During the coating deposition, the influence of deposition time on the weight gain of SGG1/PEEK and SGG2/PEEK coatings was investigated. The results show that the deposited weight increases nearly linearly with deposition time and causes a decrease in current density due to increased electrical resistance (Figures 5(a) and (b), respectively). The as-deposited (green) coatings were composed of the SGG and PEEK powders not connected with each other, which influenced the significant impact on the poor as-deposited coating adhesion to the substrate. To densify the green coatings and to increase their adhesion to the alloy substrate, the

as-coated alloy was post-deposition heated at a temperature of 628 K (355 °C) for 20 minutes. Such treatment allowed the PEEK powder to melt and contributed to the improvement of the coating adhesion to the underlying titanium alloy.

B. Microstructure of the SGG/PEEK Coatings

SEM investigation confirmed the results of visual observation of the coating uniformity and showed that the green SGG1/PEEK and SGG2/PEEK coatings were composed of homogeneously distributed SGG and PEEK particles (Figures 6(a) and (b)). Figures 7(a) and (b) show the surface morphology of the SGG1/PEEK and SGG2/PEEK coatings after heating at 628 K (355 °C) for 20 minutes. Both coatings are microporous with pores distributed homogeneously over the coatings. Heated SGG1/PEEK coatings exhibited a homogeneous microstructure with uniformly distributed microcracks (Figure 7(a)). A net of microcracks also occurred in the surface of heated SGG2/PEEK coatings (Figures 7(b) and (c)). In contrast to the SGG1/PEEK coating, the deep microcracks were observed in this coating which bared to reveal the underlying substrate material (Figure 7(c)). Their widths were measured and found to be up to 15 μm. Sato *et al.*^[38] reported that particle size has an influence on the formation of cracks in the EPD deposit during drying. They found that the volume fraction of cracks in coatings deposited from suspensions consisting of relatively small particles (0.06 μm) was much less than that in coatings deposited from the suspension containing larger particles (3 μm). In our coatings, the cracks were not observed in green deposits, but these were formed during the cooling after heating. The greater diameter of SGG2 particles contributed to the formation of deep microcracks in SGG2/PEEK coatings.

The thicknesses of both types of coatings measured by a profilometer were similar ranging from 40 to 50 μm.

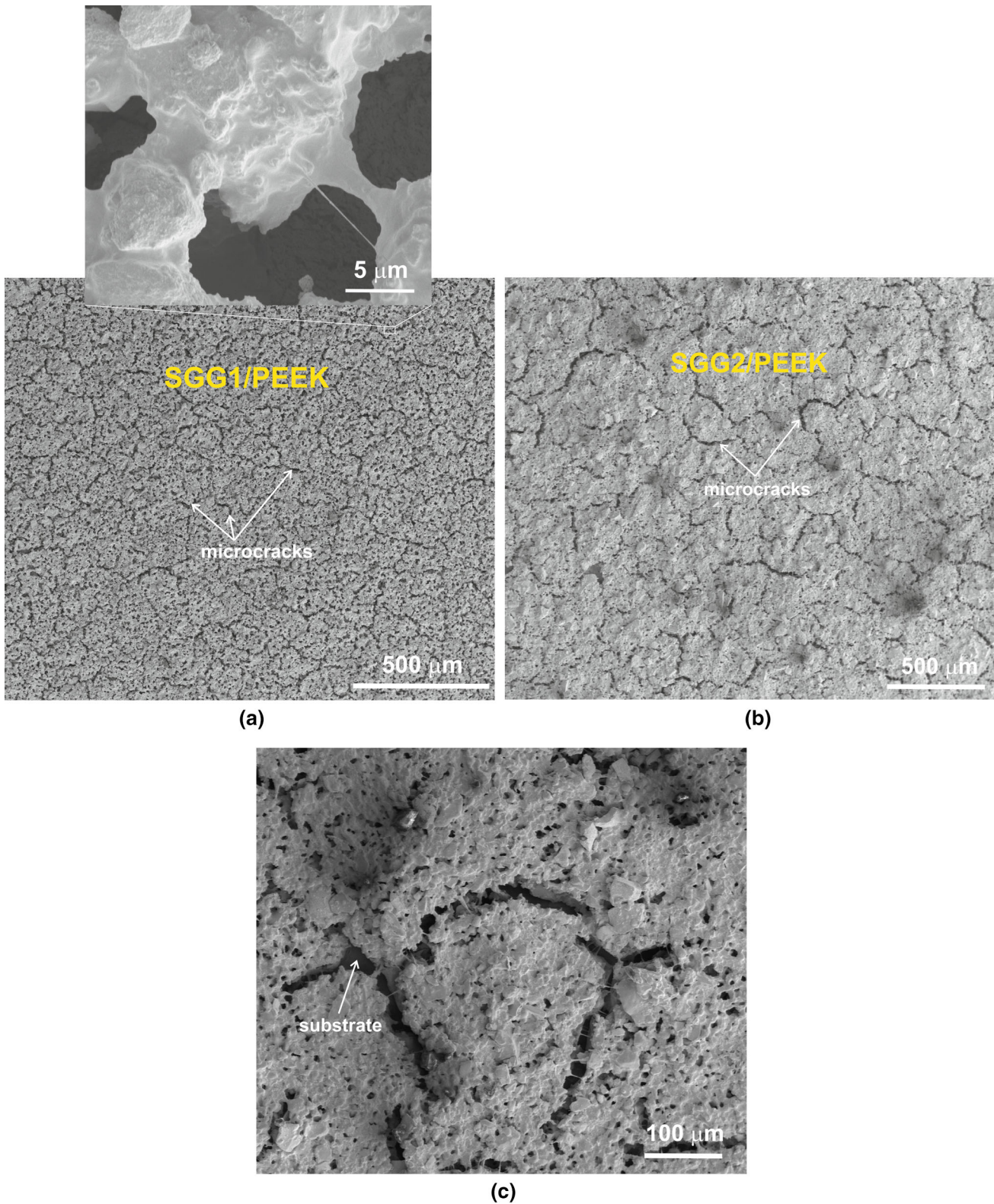


Fig. 7—SEM SE micrographs of the heated SGG1/PEEK (a) and SGG2/PEEK (b, c) coatings on the Ti-13Nb-13Zr alloy. An inset in the figure shows the magnified details of SGG1 particles embedded in the PEEK matrix.

Both coatings consist of SGG particles, with ECD up to 45 μm and up to 85 μm , respectively, embedded in a PEEK matrix. XRD investigation of the SGG1/PEEK

coating revealed the presence of the following phases: HA (hp), CaSiO_3 (tp), and PEEK (orthorhombic, space group Pbcn) (Figure 8). The presence of a small amount

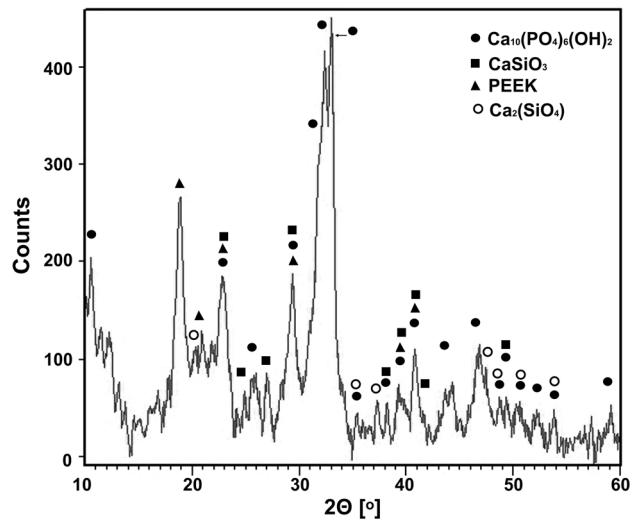


Fig. 8—XRD pattern of the SGG1/PEEK coating on the Ti-13Nb-13Zr alloy and its identification.

of Ca_2SiO_4 (op) is also possible, and the positions of main diffraction peaks for this phase were also indicated in the XRD pattern. An increase in the PEEK crystallinity after heating compared with the green coatings was observed.

A representative micrograph of the SGG1/PEEK microstructure of the coating observed by TEM is shown in Figure 9. The SAED investigation confirmed the occurrence of nanocrystalline HA (hp) particles, amorphous glass particles, and amorphous PEEK in the coating. As a result of heating at a temperature above the PEEK melting point, the particles were embedded in a polymer, which formed a durable matrix. The TEM-EDS microanalysis of chemical composition of amorphous glass particles exhibited the presence mainly of Ca, Si, and O, as well as some P. STEM-EDS line microanalysis confirmed the enrichment of Ca, Si, O, and P in sol-gel glass particles as well as C and O in the PEEK matrix (Figure 10). Contrary to our observation in previous investigation on porous Bioglass/PEEK coatings,^[33] where diffusion of Na from the glass to the PEEK matrix after heating was found, no diffusion of any elements from SGG to PEEK was observed in this study.

Both, the SGG1/PEEK and SGG2/PEEK coatings, were highly porous with pore diameters being up to 35 and 90 μm , respectively. The mean open porosities determined by hydrostatic weighing based on the Archimedes principle were equal to 45 ± 2 and 48 ± 2 pct for SGG1/PEEK and SGG2/PEEK, respectively.

Figure 11 shows the results of FIB-SEM tomographic technique application for the visualization of structural features (pores and SGG1 particles) in porous SGG1/PEEK coating. Visualization in 3D of a tomographic reconstructed volume $18.1 \times 13.1 \times 8.6 \mu\text{m}$ allowed the imaging of open pores and sol-gel glass particles (Figure 11(a)). Figure 11(b) shows enlarged selected cross sections of pores. Sol-gel particles with the size of about a few micrometers are observed in the PEEK

polymer matrix region (area between the pore). 3D visualization of the surface topography for a reconstructed sample volume with a highly developed surface containing open pores is shown in Figure 11(c). 3D visualization of a tomographic reconstructed volume $6.5 \times 8.6 \times 6.3 \mu\text{m}$ (enlarged part of the reconstructed volume presented in Figure 11(a)) with visible interconnected pores is shown in Figure 11(d). The high open porosity of coatings is important for osteointegration of the coated implant with bone tissue.^[8,9] Macropores on or inside the material can intensify the ingrowth of tissue.^[39] Sufficient porosity, especially the presence of interconnected pores, determines the ability of bone graft materials to faster ingrowth and osteointegration. According to He *et al.*,^[40] pore sizes of at least 100 μm are sufficient for osteoid formation and ingrowth. In general, a porous coating promotes bone cell adhesion.^[41] Micropores can enhance the circulation of interstitial fluid between macropores and micropores.^[40] Micropores in the size range of 1-20 μm might promote the adhesion, spreading, and proliferation of osteoblasts.^[42] Those small pores help in the adsorption of bone-inducing protein as well as facile diffusion of nutrients and other components of physiological fluids, ion exchange, and bone formation.^[42] Bignon *et al.*^[14] reported that microporosity (0.3 to 2 μm) promotes the cytoplasmic extension to enhance the cell spreading. They also found that both macroporosity and macrointerconnectivity sizes influenced the penetration of cells. An interconnection size of 15 μm appeared to be effective to support cell ingrowth without bringing down mechanical strength.

C. Adhesion of the Coatings to the Ti-13Nb-13Zr Alloy Substrate

The basic requirement for coated biomaterials is strong coating adhesion to the underlying substrate. A quantitative measure of coating adhesion (critical load) was performed by microscratch tests. It was found that the diameters of the particles present in the coating and microcracks strongly influence the SGG/PEEK coating adhesion to the substrate. The SGG1/PEEK coating exhibited good adhesion to the Ti-13Nb-13Zr alloy substrate. The first adhesive cracks occurred in the coating after scratching under the loads $L_{c2} = 9 \text{ N}$ (Figure 12(a)). The SGG2/PEEK coating exhibited much lower adhesion to the substrate material, compared with SGG1/PEEK coatings. Adhesive cracks were present after scratching under the load $L_{c2} = 4 \text{ N}$ (Figure 12(b)). Wear products have been found in the area of the scratch track of both coatings, with more of them found in the SGG2/PEEK-coated alloy. It is clearly visible in Figure 12 that the SGG2/PEEK coating is much more brittle than the SGG1/PEEK one. The better adhesion of the SGG1/PEEK coating to the substrate is due to differences in particle size and lower degree of microcracks. The adhesion of the SGG1/PEEK coating was also better than that reported in the literature for porous bioglass/PEEK coatings.^[33] This observation indicates that particle morphology might be of great importance. Both the melted bioglass

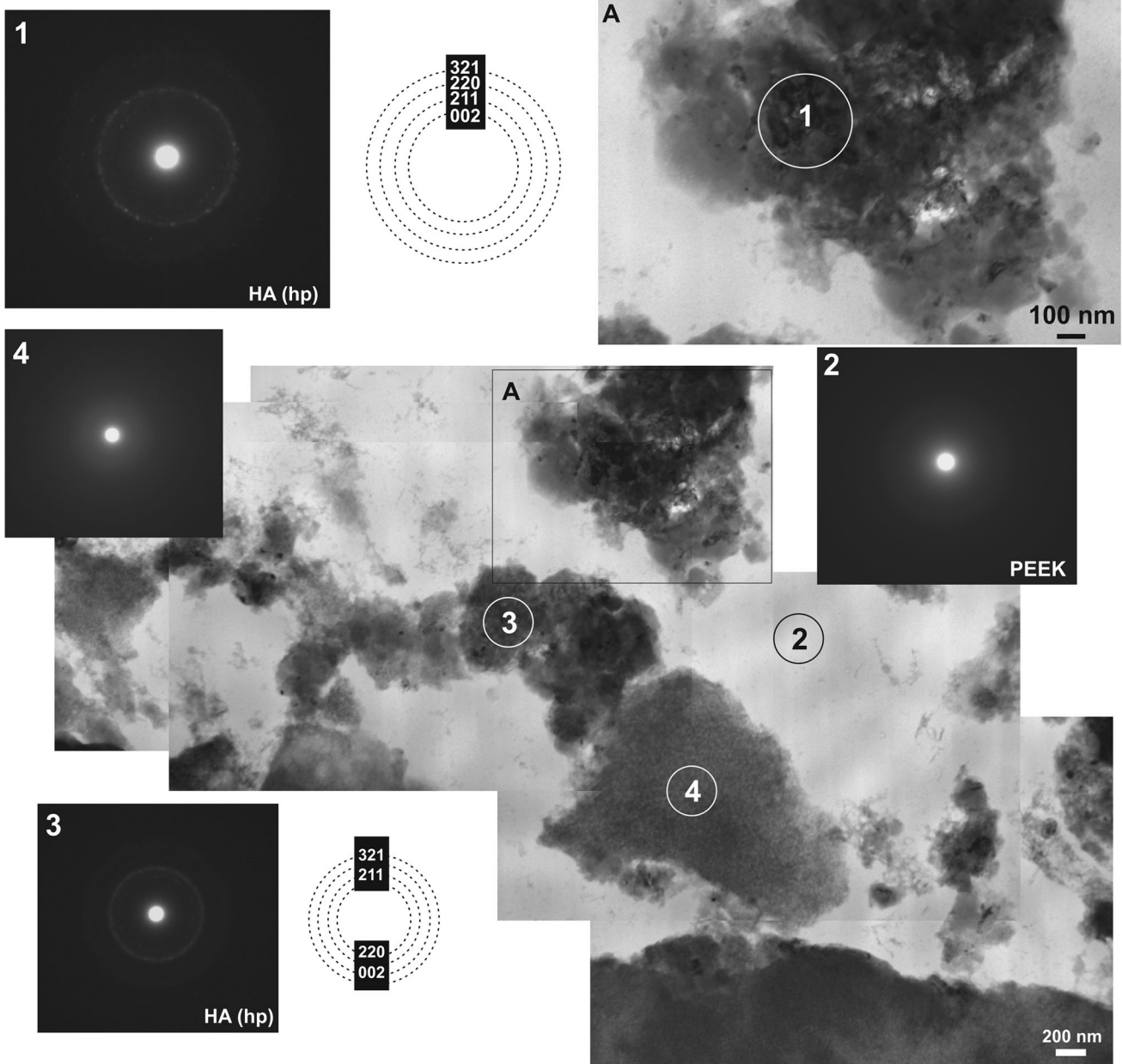


Fig. 9—Microstructures of the SGG1/PEEK coating (TEM bright-field image) and SAED patterns taken from the areas marked in the figure as 1-4 as well as their identification.

45S5 and SGG particles exhibited irregular morphology, but bioglass particles had sharp edges, while the sol-gel glass particles had high specific surface area and nanoporosity. Moreover, there are differences in the chemical compositions and structures between the bioglass and the SGG. Bioglass contains sodium and exhibits an amorphous structure, while SGG does not contain sodium and reveals a semicrystalline structure.

D. Corrosion Resistance

Due to the better adhesion of the SGG1/PEEK coating to the substrate, the electrochemical corrosion resistance was investigated only for the SGG1/PEEK

coated alloy and was compared with the uncoated alloy. Figure 13(a) shows the evolution of the open-circuit potential (OCP) for the uncoated and SGG1/PEEK coated Ti-13Nb-13Zr alloy. OCP for the SGG1/PEEK coated specimen obtained the value of -0.30 V. The observed shift in OCP to positive values for the SGG1/PEEK coated alloy may indicate a reduction in the driving force for the corrosion process.^[43] Thus, the obtained results suggest that the SGG1/PEEK coating has improved its corrosion behavior in comparison with the uncoated one. The examined materials are characterized by similar potentiodynamic polarization curves (Figure 13(b)). Because of the absence of linear regions, the Tafel extrapolation is not applicable to interpret the

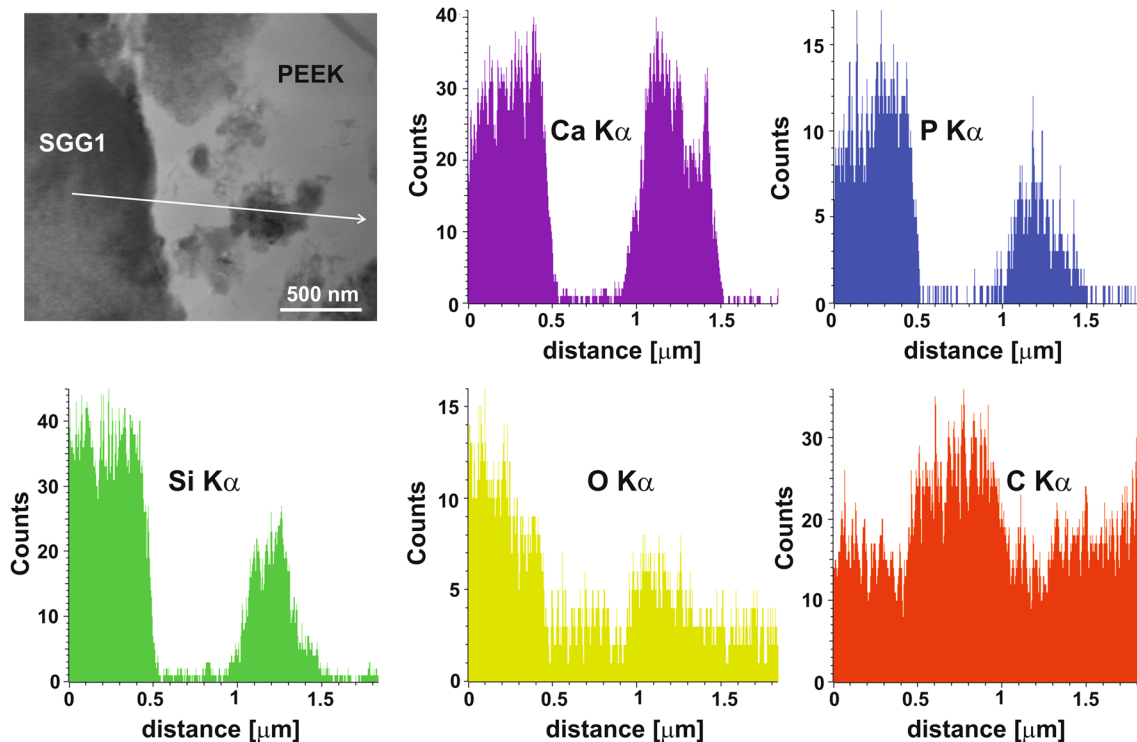


Fig. 10—STEM-EDS line profiles of Ca, Si, P, O, and C distributions in the area of the SGG1/PEEK coating along the line marked in the figure.

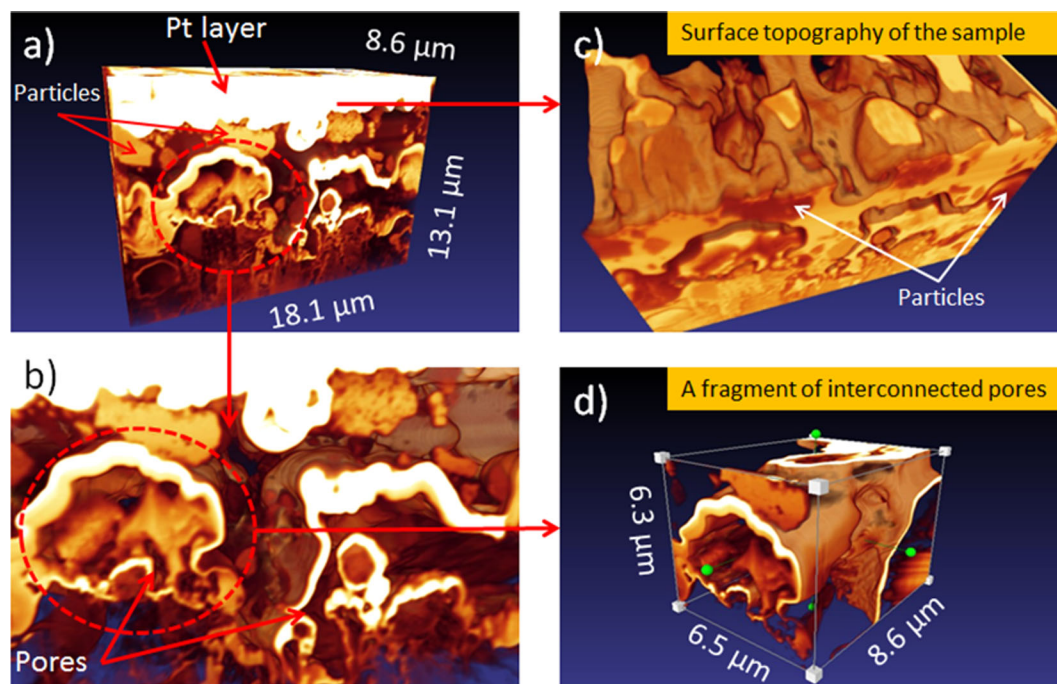


Fig. 11—3D visualization of FIB-SEM tomographic reconstruction results carried out on the open porous SGG1/PEEK coating: (a) 3D visualization of the tomographic reconstructed volume $18.1 \times 13.1 \times 8.6 \mu\text{m}$ —open pores, and sol-gel glass particles are visible; (b) imaging an enlarged fragment of the reconstructed volume—open pores visible; (c) 3D visualization of surface topography for reconstructed sample—highly developed surface visible; (d) 3D visualization of the magnified part of the tomographic reconstructed volume $6.5 \times 8.6 \times 6.3 \mu\text{m}$ —interconnected pores are visible.

electrochemical response. In such cases, the corrosion rate can be defined by the limiting current density which passes through the passivating film, thus becoming a

measure of the film's protective performance.^[44] The passive current density (i_p) was reduced from $25 \mu\text{A}/\text{cm}^2$ for the SGG1/PEEK coating on the Ti-13Nb-13Zr alloy

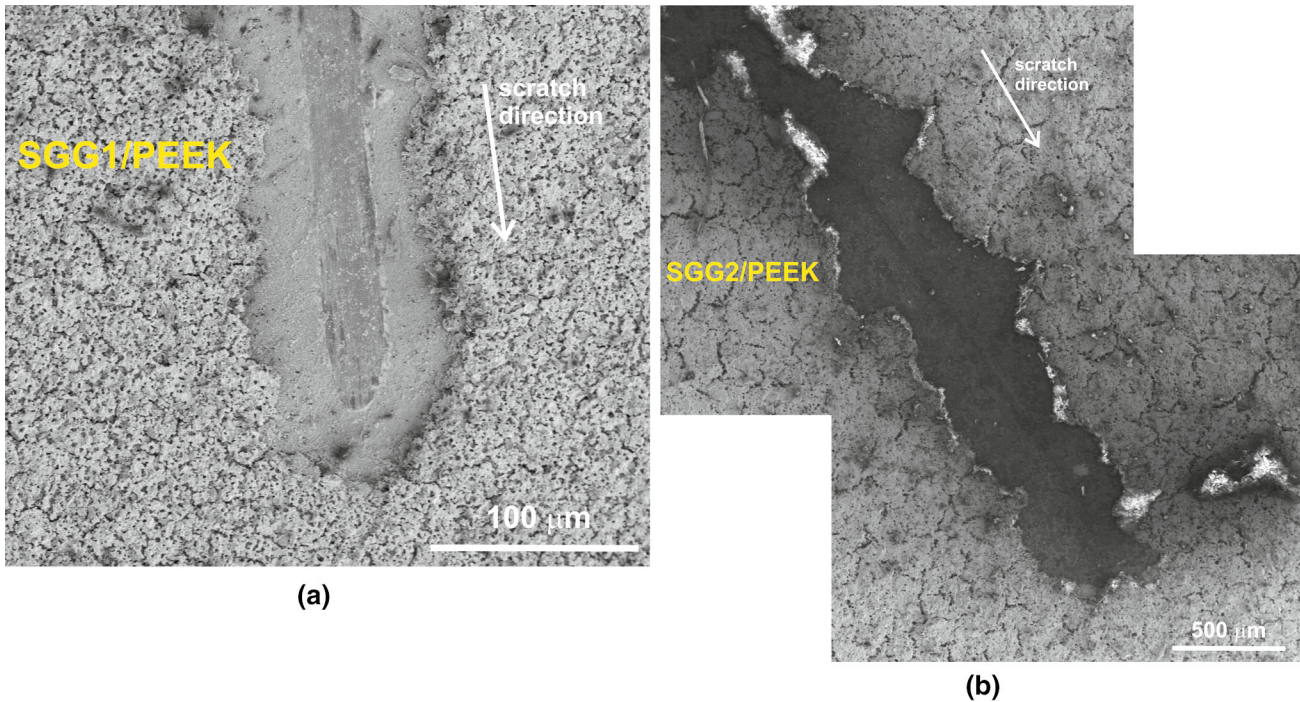


Fig. 12—SEM SE micrographs of the (a) SGG1/PEEK and (b) SGG2/PEEK coatings on the Ti-13Nb-13Zr titanium alloy after microscratch tests at loads of 9 and 4.6 N, respectively.

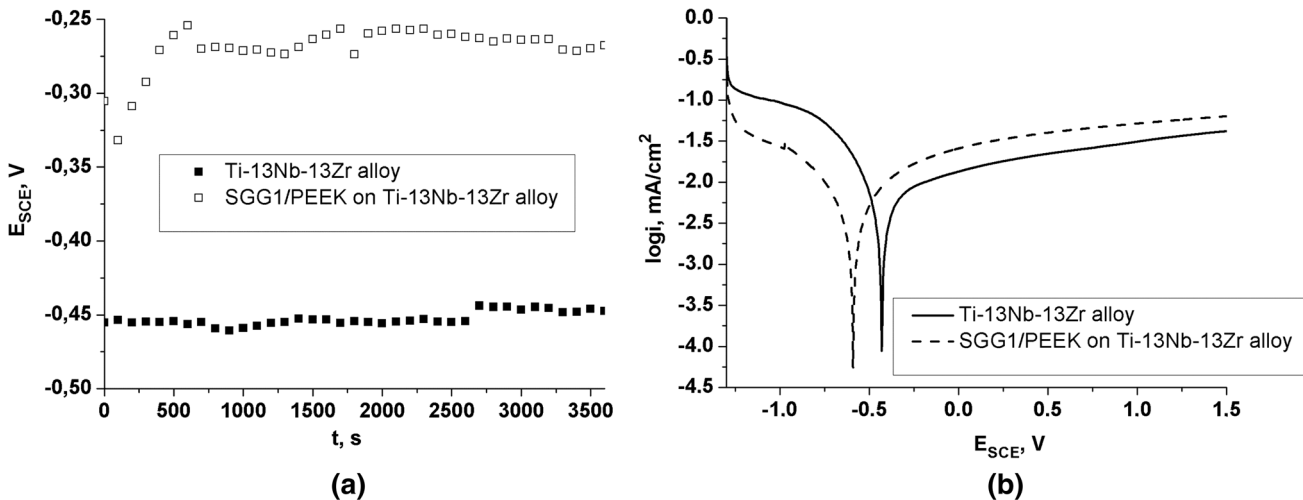


Fig. 13—Results of electrochemical measurements of the uncoated and coated Ti-13Nb-13Zr alloys in Ringer’s solution at 310 K (37 °C): (a) evolution of the corrosion potential vs time and (b) polarization curves at 1 mV/s.

to 20 $\mu\text{A}/\text{cm}^2$ for the uncoated alloy, while the potential of the cathodic–anodic transition decreased from approximately -0.30 to -0.43 V, respectively. The passive state for corrosion resistance and reasonably small variations in the passive current density in the considered cases can be neglected. A significant shift in the potential of the cathodic–anodic transition expands the passive region for the SGG1/PEEK coating on the Ti-13Nb-13Zr alloy and improves the corrosion resistance of the SGG1/PEEK coating.

Figures 14(a) through (c) shows the EIS spectra presented as a Nyquist plot (Figure 14(a)) and a Bode plot (Figures 14(b) and (c)) of the uncoated- and coated alloys in Ringer’s solution. As seen from Figure 13(b), the higher Z modulus at a lower frequency in the Bode impedance plot indicated the better corrosion resistance of the coated alloy. As seen from Figure 14(c), the uncoated and coated alloys showed highly capacitive behaviors from medium-to-low frequencies, indicating that a stable film was formed on the substrate. The

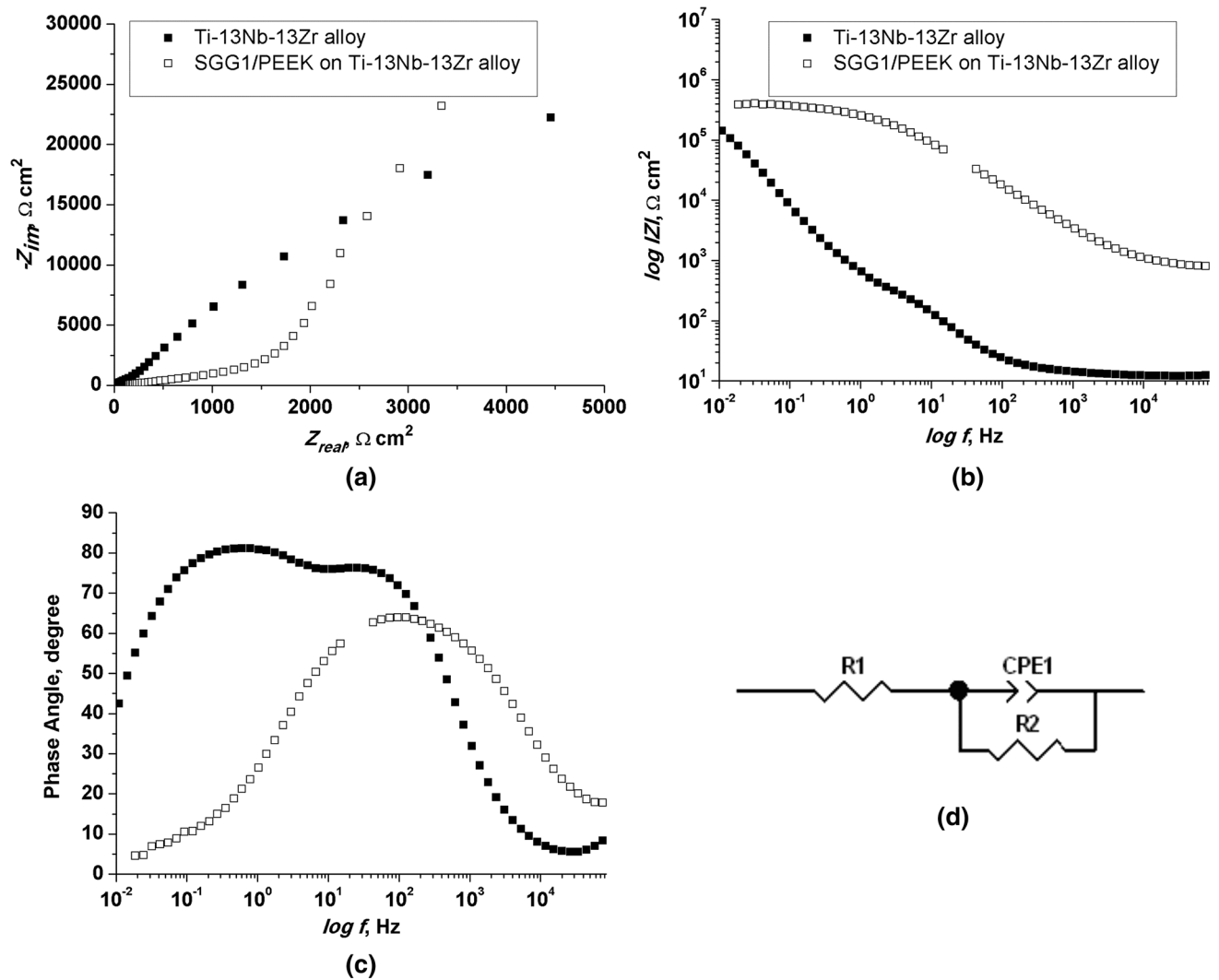


Fig. 14—Electrochemical impedance curves of the uncoated and coated alloys in Ringer’s solution: (a) Nyquist impedance plot, (b) Bode impedance plot, (c) Bode phase angle plot, (d) equivalent circuit used for fitting EIS data of investigated samples.

Table I. EIS Fitting Results Obtained from EIS Data

Samples	OCP (V)	R_1 ($\Omega \text{ cm}^2$)	CPE-T ($\text{Fs}^{n-1} \text{ cm}^{-2}$)	CPE-P	R_2 ($\Omega \text{ cm}^2$)
Ti-13Nb-13Zr alloy	-0.45	20.41	3.8235×10^{-5}	0.8142	296,660
SGG1/PEEK on Ti-13Nb-13Zr alloy	-0.30	34.84	6.5334×10^{-6}	0.8893	334,130

equivalent circuit shown in Figure 14(d) was used to fit the EIS data. According to the double-layer model for the surface coating, the equivalent circuit consisted of the electrolyte resistance (R_1), the coating resistance (R_2), and the constant-phase elements (CPEs). A good fit between the experimental and simulated results was achieved, and the circuit parameters are listed in Table I.

The SGG1/PEEK coating on the Ti-13Nb-13Zr alloy had a slightly higher CPE-P value which was closest to the capacitance (typical of passive coatings). The resistance (R_2) of the SGG1/PEEK coating on the Ti-13Nb-13Zr alloy was higher than that of the

uncoated Ti-13Nb-13Zr alloy, which suggested that the SGG1/PEEK coating on the Ti-13Nb-13Zr alloy had better corrosion resistance than the uncoated alloy.

IV. CONCLUSIONS

1. Microporous SGG/PEEK coatings were successfully deposited on the Ti-13Nb-13Zr alloy by EPD. The coating homogeneity and uniformity depend strongly on the chemical composition of the suspension as well as on the electrophoretic voltage and time. The best-quality, homogeneous coatings

were deposited from a suspension composed of 3.2 g sol-gel glass, 1 g PEEK, and 5 g of citric acid in EtOH at a potential difference of 50 V for 120 seconds.

- The thicknesses of both types of coating were similar and in the range from 40 to 50 μm . Both the SGG1/PEEK and SGG2/PEEK coatings consist of HA (hp), CaSiO_3 (tp), a small amount of Ca_2SiO_4 (op), and amorphous glass particles, with ECDs of up to 45 μm and up to 85 μm , respectively, embedded in a semicrystalline PEEK matrix. The PEEK crystallinity increased as a result of heating of the coated specimens above the PEEK melting point.
- Both the SGG1/PEEK and SGG2/PEEK coatings were highly porous with pore diameters up to 35 μm and up to 90 μm , respectively. The mean volumetric open porosities, determined by hydrostatic weighing based on the Archimedes principle, were 45 and 48 pct, respectively.
- The SGG1/PEEK coating exhibited very good adhesion to the titanium alloy substrate. The first adhesive cracks were observed after scratching under a load of 9 N. The SGG2/PEEK coating exhibited lower adhesion to the substrate due to the presence of large-sized SGG particles and deep microcracks bared to reveal the underlying substrate material.
- The SGG1/PEEK coated alloy exhibited better corrosion resistance in Ringer's solution compared with the uncoated alloy. This results from coating uniformity and homogeneity as well as its very good adhesion to the substrate material.

This study shows that electrophoretic deposition is very useful to deposit microporous composite sol-gel glass/PEEK coatings well adhered to titanium alloy substrates used in medical applications, and also improve the corrosion resistance of titanium alloy in Ringer's solution.

ACKNOWLEDGMENTS

This study was supported by the Polish National Science Centre (decision no. DEC-2013/09/B/ST8/00145). The authors appreciate the valuable contribution of Dr Ł. Cieniek (AGH University of Science and Technology) to SEM and DSc M. Kot (AGH-UST) during scratch tests.

OPEN ACCESS

This article is distributed under the terms of the Creative Commons Attribution 4.0 International License (<http://creativecommons.org/licenses/by/4.0/>), which permits unrestricted use, distribution, and reproduction in any medium, provided you give appropriate credit to the original author(s) and the source,

provide a link to the Creative Commons license, and indicate if changes were made.

REFERENCES

- P.S. Nnamchi, C.S. Obayi, I. Todd, and M.W. Rainforth: *J. Mech. Behav. Biomed. Mater.*, 2016, vol. 60, pp. 68–77.
- K.P. Ananth, S. Suganya, S. Mangalaraj, J.M.F. Ferreira, and A. Balamurugan: *Mat. Sci. Eng. C*, 2013, vol. 33, pp. 4160–66.
- J. Qian, K. Farokhzadeh, and A. Edrissy: *Surf. Coat. Technol.*, 2014, vol. 258, pp. 134–41.
- M. Long and H.J. Rack: *Biomaterials*, 1998, vol. 19, pp. 1621–39.
- M. Geetha, A.K. Singh, R. Asokamani, and A.K. Gogia: *Prog. Mater. Sci.*, 2009, vol. 54, pp. 397–425.
- X. Liu, P.K. Chu, and Ch. Ding: *Mater. Sci. Eng. R*, 2004, vol. 47, pp. 49–121.
- T.J. Webster, A.A. Patel, M.N. Rahaman, and B.S. Bal: *Acta Biomater.*, 2012, vol. 8, pp. 4447–54.
- M. Mehdipour and A. Afshar: *Ceram. Int.*, 2012, vol. 38, pp. 471–76.
- D.J. Trantolo, M.J. Yaszemski, K. Lewandrowski, V. Hasirci, D.E. Altobelli, and D.L. Wise: *Macel Dekker, Inc, Biomaterials in Orthopedics*. 2004. pp. 401–37.
- A.R. Boccaccini and J.E. Gough: *Tissue Engineering Using Ceramics and Polymers*, CRC Press, Boca Raton, 2007, pp. 1–114.
- S.F. Hulbert, F.A. Young, R.S. Mathews, J.J. Klawitter, C.D. Talbert, and F.H. Stelling: *J. Biomed. Mater. Res. Part B*, 1970, vol. 4, pp. 433–56.
- J.O. Hollinger, J. Brekke, E. Gruskin, and D. Lee: *Clin. Orthop. Relat. Res.*, 1996, vol. 324, pp. 55–65.
- Ch. Hadjicharalambous, O. Prymak, K. Loza, A. Buyakov, S. Kulkov, and M. Chatzinikolaïdou: *Front. Bioeng Biotechnol.*, 2015, vol. 3, pp. 1–10.
- A. Bignon, J. Chouteau, J. Chevalier, G. Fantozzi, J.-P. Carret, P. Chavassieux, G. Boivin, M. Melin, and D. Hartmann: *J. Mater. Sci. Mater. Med.*, 2003, vol. 14, pp. 1089–97.
- A.R. Boccaccini, C. Peters, J.A. Roether, D. Eifler, S.K. Misra, and E.J. Minay: *J. Mater. Sci.*, 2006, vol. 41, pp. 8152–59.
- I. Corini, N. Neuman, and A.R. Boccaccini: *Adv. Eng. Mater.*, 2008, vol. 10, pp. 559–64.
- A.R. Boccaccini, J.A. Roether, J.C. Thomas, S.P. Shaffer, E. Chavez, E. Stoll, and E.J. Minay: *J. Ceram. Soc. Jpn.*, 2006, vol. 11, pp. 1–14.
- A.R. Boccaccini and I. Zhitomirsky: *Curr. Opin. Solid State Mater. Sci.*, 2002, vol. 6, pp. 251–60.
- J. Ma, C.H. Liang, L.B. Kong, and C. Wang: *J. Mater. Sci. Mater. Med.*, 2003, vol. 14, pp. 797–801.
- M. Javidi, S. Javadpour, M.E. Bahrololoom, and J. Ma: *Mater. Sci. Eng. C*, 2008, vol. 28, pp. 1509–15.
- L. Petrovic, D. Pohle, H. Munstedt, T. Rechtenwald, K.A. Schlegel, and S. Rupprecht: *J. Biomed. Sci.*, 2006, vol. 13, pp. 41–46.
- Z.P. Lu and K. Friedrich: *Wear*, 1995, vol. 181, pp. 624–31.
- G. Zhang, H. Liao, M. Cheriguj, J.P. Davim, and C. Coddet: *Eur. Polym. J.*, 2007, vol. 43, pp. 1077–82.
- L.C. Gerhardt and A.R. Boccaccini: *Materials*, 2010, vol. 3, pp. 3867–3910.
- L.L. Hench: *J. Am. Ceram. Soc.*, 1998, vol. 81, pp. 1705–28.
- L.L. Hench: *J. Mater. Sci. Mater. Med.*, 2006, vol. 17, pp. 967–78.
- M. Dziadek, B. Zagrajczuk, E. Menaszek, and A. Wegrzynowicz: *Ceram. Int.*, 2016, vol. 42, pp. 5842–57.
- S. Seuss, M. Heinloth, and A.R. Boccaccini: *Surf. Coat. Technol.*, 2016, vol. 301, pp. 100–05.
- A. Hoppe, N.S. Güldal, and A.R. Boccaccini: *Biomaterials*, 2011, vol. 32, pp. 2757–74.
- S.K. Misra, D. Mohn, T.J. Brunner, W.J. Strark, S.E. Philip, I. Roy, V. Salih, C. Knowles, and A.R. Boccacini: *Biomaterials*, 2008, vol. 29, pp. 1750–61.
- E. Pamała, J. Kokoszka, K. Cholewa-Kowalska, M. Łączka, Ł. Kantor, Ł. Niedzielski, G.C.J. Reilly, J. Filipowska, W. Madej, M. Kołodziejczyk, G. Tylko, and A.M. Osyczka: *Ann. Biomed. Eng.*, 2011, vol. 39, pp. 2114–29.

32. J. Wilson, G.H. Pigott, F.J. Schoen, and L.L. Hench: *J. Biomed. Mater. Res. A*, 2004, vol. 15, pp. 805–17.
33. T. Moskalewicz, S. Seuss, and A.R. Boccaccini: *Appl. Surf. Sci.*, 2013, vol. 273, pp. 62–67.
34. A. Sak, T. Moskalewicz, S. Zimowski, Ł. Cieniek, B. Dubiel, A. Radziszewska, M. Kot, and A. Łukaszczyk: *Mat. Sci. Eng. C*, 2016, vol. 63, pp. 52–61.
35. ISO 2738: 1999, *Sintered metal materials excluding hardmetals. Permeable sintered metal materials. Determination of density, oil content and open porosity*, <http://www.iso.org>. Accessed 5 Dec 2016.
36. M. Ammam: *RSC Adv.*, 2005, vol. 2, pp. 7633–46.
37. L. Besra and M. Liu: *Prog. Mater. Sci.*, 2007, vol. 52, pp. 1–61.
38. N. Sato, M. Kawachi, K. Noto, N. Yoshimoto M. Yoshizawa: *Physica C*, 2001, vols. 357–360, pp. 1019–22.
39. Z. Shi, X. Huang, Y. Cai, R. Tang, and D. Yang: *Acta Biomater.*, 2009, vol. 5, pp. 338–45.
40. G. He, J. Hu, S.C. Wie, J.H. Li, X.H. Liang, and E. Luo: *Appl. Surf. Sci.*, 2008, vol. 255, pp. 442–45.
41. X. Liu, M. Li, Y. Zhu, K.W.K. Yeung, P.K. Chu, and S. Wu: *Bioact. Mater.*, 2016, vol. 1, pp. 65–76.
42. M. Śmiga-Matuszowicz, B. Janicki, K. Jaszcz, J. Łukaszczyk M. Kaczmarek, M. Lesiak, A.L. Sieroń, W. Simka, M. Mierzwiński, and D. Kusze: *Mater. Sci. Eng. C*, 2014, vol. 45, pp. 64–71.
43. D.J. Blackwood, A.W. Chua, and K.H.W. Seah: *Corr. Sci.*, 2000, vol. 42, pp. 481–503.
44. E. Mc Cafferty and G.K. Hubler: *J. Electrochem. Soc.*, 1978, vol. 11, pp. 1892–93.